UNIVERSITY OF BIRMINGHAM

University of Birmingham Research at Birmingham

An investigation on nitrogen uptake and microstructure of equimolar quaternary FeCoNiCr high entropy alloy after active-screen plasma nitriding

Tao, Xiao; Yang, Yepeng; Qi, Jiahui; Cai, Biao; Rainforth, W. Mark; Li, Xiaoying; Dong, Hanshan

Link to publication on Research at Birmingham portal

An investigation on nitrogen uptake and microstructure of equimolar quaternary FeCoNiCr high entropy alloy after active-screen plasma nitriding

Xiao Tao [a,c,*], Yepeng Yang [a], Jiahui Qi [b], Biao Cai [a], W. Mark Rainforth [b], Xiaoying Li [a], Hanshan Dong [a]

[a] School of Metallurgy and Materials, University of Birmingham, B15 2TT, United Kingdom
[b] Department of Materials Science and Engineering, University of Sheffield, S1 3JD, UK
[c] Jiangsu Key Laboratory of Advanced Metallic Materials, School of Materials Science and Engineering, Southeast University, Nanjing 211189, China

ABSTRACT

Under nitrogen diffusion treatments, N-expanded austenite (γ_N) can form at the surface of self-passivating Fe-Cr, Ni-Cr, and Co-Cr alloys at low temperatures, which provides beneficial hardening and enhancements in wear resistance without reducing corrosion resistance. Given the wide research interests in multicomponent equimolar alloys, an equimolar quaternary FeCoNiCr high entropy alloy (HEA) was investigated after active-screen plasma nitriding at 430–480 °C in this study. Firstly, the formation of γ_N-FeCoNiCr case at 430 °C was demonstrated with the bright case appearance after metallographic etching, the lattice expansion under XRD, the FCC electron diffraction patterns and the shear bands under TEM. Secondly, the thick treatment cases at ~9–16 μm first indicated that N interstitial diffusion was not sluggish in the FeCoNiCr surface. Thirdly, analogous to stainless steels, the onset of dark regions in the etched γ_N-FeCoNiCr case was owing to the formation of a cellular mixture of CrN + γ-(Fe, Co, Ni) nano-lamellae at elevated treatment temperatures. The residual bright regions in γ_N-FeCoNiCr at 480 °C showed ~1–3 nm CrN nanoprecipitates with no substantial Cr segregation. Additionally, a significant nanocrystalline layer was seen at the topmost surface at 480 °C, which is most likely associated with the high substrate Cr content.

1. Introduction

Following the early works by Zhang and Bell [1] and Ichii et al. [2] in the late 1980s, an interstitial-supersaturated and anisotropically expanded phase – known as S-phase or expanded austenite (denoted as γ_N/γ_C) – has been extensively investigated at the surface of austenitic stainless steels (SSs) after low-temperature nitriding/carburising treatments, which can provide beneficial enhancements in material wear and fatigue performance without compromising corrosion resistance [3–7]. The study on N-expanded austenite (γ_N) cases has now been extended to a wide range of substrate alloys, including Fe-Cr-Ni/Mn SSs [6,8–10], Co alloys [11–13], Ni-superalloys [14–18], etc. Interstitial-expanded austenite is featured with the "colossal" [19] interstitial absorption (and the associated anisotropic lattice expansion and high residual stress) and the absence of nitride precipitates owing to prohibited

substitutional diffusion at the low treatment temperatures. However, at elevated treatment temperatures, the high chemical affinity between Cr and N in γ_N can drive Cr segregation, which results in reduced corrosion resistance at treatment temperatures ranging from approximately 400–500 °C (the exact threshold treatment conditions vary with the substrate alloy and treatment time) [4,5,20,21].

The effects of the alloying elements in the substrate composition on the surface diffusion case have been investigated. The different components in the chemical composition of the 'conventional' alloys (such as Fe-Cr-Ni/Mn SS) play different roles in the formation, interstitial absorption, microstructure evolution and decomposition of expanded austenite. Firstly, a high Cr content appears crucial for colossal supersaturation and anisotropic lattice expansion by providing sufficient interstitial trap sites [22–24]. Secondly, both Mn and Ni, while having relatively weaker chemical affinity to N (compared to Cr, in Fe-Cr-Ni/

Mn SSs), can influence the lattice plasticity mechanism under the N-induced strain and the nanostructure of the expanded austenite case [10,25,26]. Thirdly, the predominant matrix elements of the substrate (i.e., Fe, Ni and Co) also influence the thickness and interstitial absorption levels of the expanded austenite case [27].

Since the early studies by Cantor et al. [28] and Yeh et al. [29] in the early 2000s, a new group of alloys composed of equimolar chemical elements – high entropy alloy (HEA) – has raised wide research interests and shown attractive material property combinations for various engineering applications [30,31]. Given that expanded austenite formed in Fe-Cr, Ni-Cr and Co-Cr alloys [27], a large number of high-Cr face-centred cubic (FCC) HEAs – such as FeCoNiCr, FeCoNiMnCr, FeCoNiCuCr and their derivatives (e.g., FeCoNiCrCu$_{0.5}$, FeCoNiCrMo$_{0.3}$, FeCoNiCrAl$_{0.3}$, etc.) [32] can benefit from the low-temperature interstitial diffusion treatments for improved surface wear performances without reducing corrosion resistance.

Concerning the large number of HEA systems and their complex chemical compositions, it is sensible to investigate the low-temperature nitriding/carburising response of the basic HEAs, such as ternary FeNiCr [33], quaternary FeCoNiCr [34], and quinary FeCoNiMnCr [35]. Empirically, γ_N has only been generated in Fe/Co/Ni-based alloys, as summarised in Ref. [27]. In this sense, the equimolar FeCoNiCr HEA is composed of the 'only' three matrix elements (i.e., Fe, Ni and Co) and the "interstitial-trapping" element (i.e., Cr) known for the formation of γ_N, making it an important reference HEA to be investigated under low-temperature carbon/nitrogen diffusion treatments before the further studies on the numerous equimolar alloys. The FeCoNiCr-based HEAs also possess excellent strength-ductility combinations at 15/77 K with great potential for cryogenic applications [36–39]. However, there is a lack of a systematic study on the low-temperature nitriding response of FeCoNiCr HEA.

In addition, one wonders the influences from the "sluggish diffusion", as being one of the "core effects" of HEAs since Yeh [40], to the γ_N case formed upon nitrogen thermochemical diffusion treatments. Despite the debates on the "sluggish diffusion" effect in HEAs [41–44], FeCoNiCr has been demonstrated to exhibit sluggish substitutional diffusion, when compared to conventional Ni, Fe-Ni and Fe-Cr-Ni alloys (i.e., Ni tracer diffusivity is significantly lower in FeCoNiCr than those in pure Ni, Fe-45Ni, and Fe-15Cr-20Ni [45]). However, the "sluggish diffusion" effect of HEA in the open literature was based on the substitutional diffusivity at elevated temperatures (e.g., > ~700 °C). There is a lack of information on elemental diffusion at temperatures below ~500 °C, where substitutional diffusion is prohibited. Therefore, in this study, an equimolar FeCoNiCr alloy was prepared and nitrided at 430–480 °C to study the surface nitrogen uptake and microstructure evolution.

2. Experimental

Equimolar FeCoNiCr alloy was synthesised by P/M technology. Powders were encapsulated and annealed (1200 °C for 1 h), followed by hot extrusion and air cooling [37]. The extruded bar was sliced into 2 mm thick discs. One side of the discs was successively ground using P400, P800 and P1200 SiC paper for plasma nitriding and characterisations. Samples were then cleaned in acetone for 15 mins in an ultrasonic bath. Material chemical composition (i.e., 24.9Fe-25.8Co-24.2Cr-25.1Ni, wt%) was confirmed via energy-dispersive X-ray spectroscopy (EDS) under a Jeol 7000 scanning electron microscope (SEM) at an acceleration voltage of 20 keV and a spot size at 11. Active screen plasma nitriding (ASPN) treatments were carried out at 430 °C, 450 °C and 480 °C for 10 h at a pressure of 0.75 mbar in 25 vol% N_2 + 75 vol% H_2. The nitriding treatments were carried out in an industrial-scale PlasmaMetal active screen unit, as previously described in [46]. The worktable was connected with a DC power that was set at 0.75 kVA during nitriding. A separate DC power at ~15–25 kVA was applied on the stainless steel active screen to reach and maintain the treatment

temperatures. Samples were cooled to <100 °C overnight in the vacuum chamber. The mean cooling rate was ~2.2 °C min^{-1} at the temperature range from 480 °C to 350 °C.

Sample denotation is based on treatment temperature, e.g., N430-HEA denotes the sample after ASPN at 430 °C. Sample cross-sections were etched in 50HCl-25HNO$_3$–25H$_2$O (vol%), which were examined under a Jeol 7000 SEM for case morphology. Surface phase compositions were examined by X-ray diffraction (XRD) analysis using a PROTO AXRD benchtop powder diffractometer (Cu-Kα, 0.154 nm). 2Theta angle, step and dwell time were 30–60°, 0.015° and 2 s, respectively. Surface hardness was evaluated using a Mitutoyo MVK-H1 hardness indenter at a load of 0.025 kg and dwell time of 10 s. The mean hardness value was averaged from 10 measurements. The composition-depth profiles of the nitrided surfaces were examined by glow discharge optical spectroscopy (GDOES) using a Spectruma GDA650HR instrument. Cross-sectional transmission electron microscopy (TEM) samples were prepared by the focused ion beam (FIB) method using an FEI Quanta 200 3D instrument (Ga$^+$, 30 kV), which involved a final polishing step using a 5 kV Ga$^+$ beam. TEM, selective area electron diffraction (SAED), and bright-field/dark-field images (BF/DF-TEM) were taken using an FEI Tecnai F20 microscope (FEG, 200 kV). Scanning TEM (STEM) and high-resolution TEM (HRTEM) were carried out in a Jeol F200 instrument (C-FEG, 200 kV). STEM-EDS was performed in Jeol F200 using 10 μm C2 aperture and a probe size of 7.

3. Results and discussion

3.1. Morphology, thickness and surface hardness

A bright case was observed in the FeCoNiCr HEA surface after ASPN at 430 °C (Fig. 1a**&b**). At 450 °C, dark regions can be observed in the vicinity of grain boundaries and the topmost region in the treatment case (Fig. 1d**&e**). At 480 °C, the dark regions increased in volume fraction and grew towards the γ_N grains from grain boundaries and the topmost surface (Fig. 1e**&f**). Dark regions in etched nitrided cases in SSs have been reported owing to significant Cr segregation under Cr-nitride precipitations at elevated nitriding temperatures (and/or prolonged treatment times) [4]. The dark regions in Fig. 1c-f hint at sginificant Cr segregation at both 450 and 480 °C. The nitrided FeCoNiCr displayed case thicknesses ranging from ~10–16 μm and surface hardness at ~1300–1400 HV$_{0.025}$ (Table 1). The case thickness and the surface hardness for the nitrided FeCoNiCr were comparable to the 2–20 μm and the 1400–1600 HV low-temperature nitrided surfaces of SSs [4,8,9].

3.2. Composition-depth profiles

All ASPN-treated surfaces showed N concentration profiles with a relatively flat high-N concentration region followed by a sharp drop at the case/substrate interface (Fig. 2). The N contents in the relatively flat high-N region range from ~20 to 28 at.% at all three treatment temperatures. This gives N occupancy at ~0.25–0.39 and N:Cr ratio at 1.00–1.56 (as calculated from atomic concentrations) for the ASPN-treated FeCoNiCr in this study, which is relatively low when compared with the N occupancy at 0.16–0.62 and N:Cr ratio at 0.83–3.2 evaluated from the low-temperature gas nitrided 304/316 SSs [47]. Very high N concentrations were observed at the topmost surface region in the GDOES profile for all nitrided FeCoNiCr, which has been attributed to the surface "contaminations" and "nitride formations" [48]. The maximum N content in this region seems to increase from ~33 to ~43 at.% with increasing treatment temperature. The "very high N concentrations" at the topmost nitrided surface in this study could be associated with excess N uptake at the topmost nanocrystalline layer (see **Section 3.4** and **Section 4.2**).
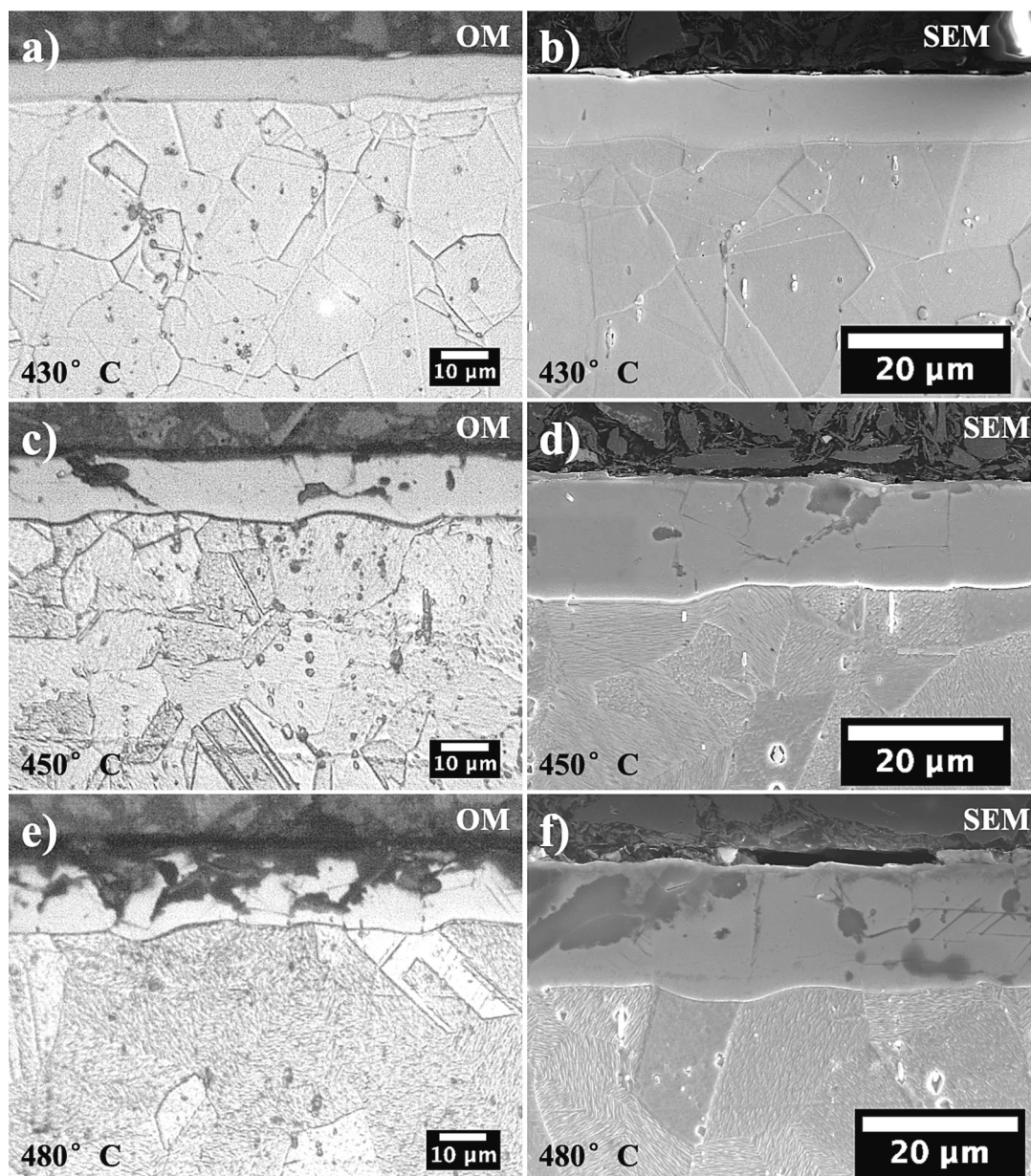
Fig. 1. OM and SEM images for cross-sectional morphology (etched in 50HCl-25HNO$_3$–25-H$_2$O, vol%) for the FeCoNiCr HEA after ASPN treatments at a-b) 430 °C, c-d) 450 °C and e-f) 480 °C.

Table 1
Case thickness and surface hardness.

Sample	Case depths, μm	Surface hardness, HV$_{0.025}$
UNT-HEA	/	237 ± 3
N430-HEA	9.4 ± 0.8	1327 ± 114
N450-HEA	13.5 ± 0.8	1395 ± 192
N480-HEA	16.2 ± 1.1	1358 ± 186

3.3. XRD analysis

Characteristic anisotropic peak shiftings were seen after all ASPN treatments. The measured peak positions were 44.0° for γ(111) and 52.1° for γ(200) on untreated FeCoNiCr, indicating lattice parameter at 0.356–0.357 nm. The systematic anisotropic XRD peak shifting indicated the formation of N-expanded austenite (as indicated in Fig. 3). The apparent lattice parameters derived from the γ$_N$(111) and γ$_N$(200) XRD

peaks at 430 °C were 0.378 nm and 0.393 nm, respectively. This suggested anisotropic lattice expansion at 6% and 10–11% for FCC 111 and 200, respectively.

The broad γ(111) peak at 450 and 480 °C corresponds to the FCC-γ in the cellular precipitation region (see Fig. 5) and the topmost nanocrystalline layer (see Fig. 7). Consistent with the small volumes of dark regions in N450-HEA (Fig. 1**c&d**), the broad γ(111) peak at 450 °C (Fig. 3) suggests the onset of γ$_N$ decomposition at 450 °C. As dark regions became more significant in the nitrided case at enhanced diffusion kinetics at 480 °C (Fig. 1**e&f**), a small hump of CrN(111) peak at 37.8° and a broad γ(111) peak at 44° were observable for N480-HEA (Fig. 3). Noticeably, the intense γ(200) and weak γ(111) XRD peak for UNT-HEA surface suggested texture, which most likely resulted from the extrusion process for the bulk HEA bar. In addition, the slight change in XRD peak intensity ratio for γ$_N$ after ASPN (i.e., increased FCC 111 peak intensity for the nitrided surfaces, Fig. 3) could be associated with the crystallographic rotation of the γ$_N$ grains towards ⟨111⟩pole under the N-induced strain, as demonstrated with γ$_N$-316 cases [49–51].
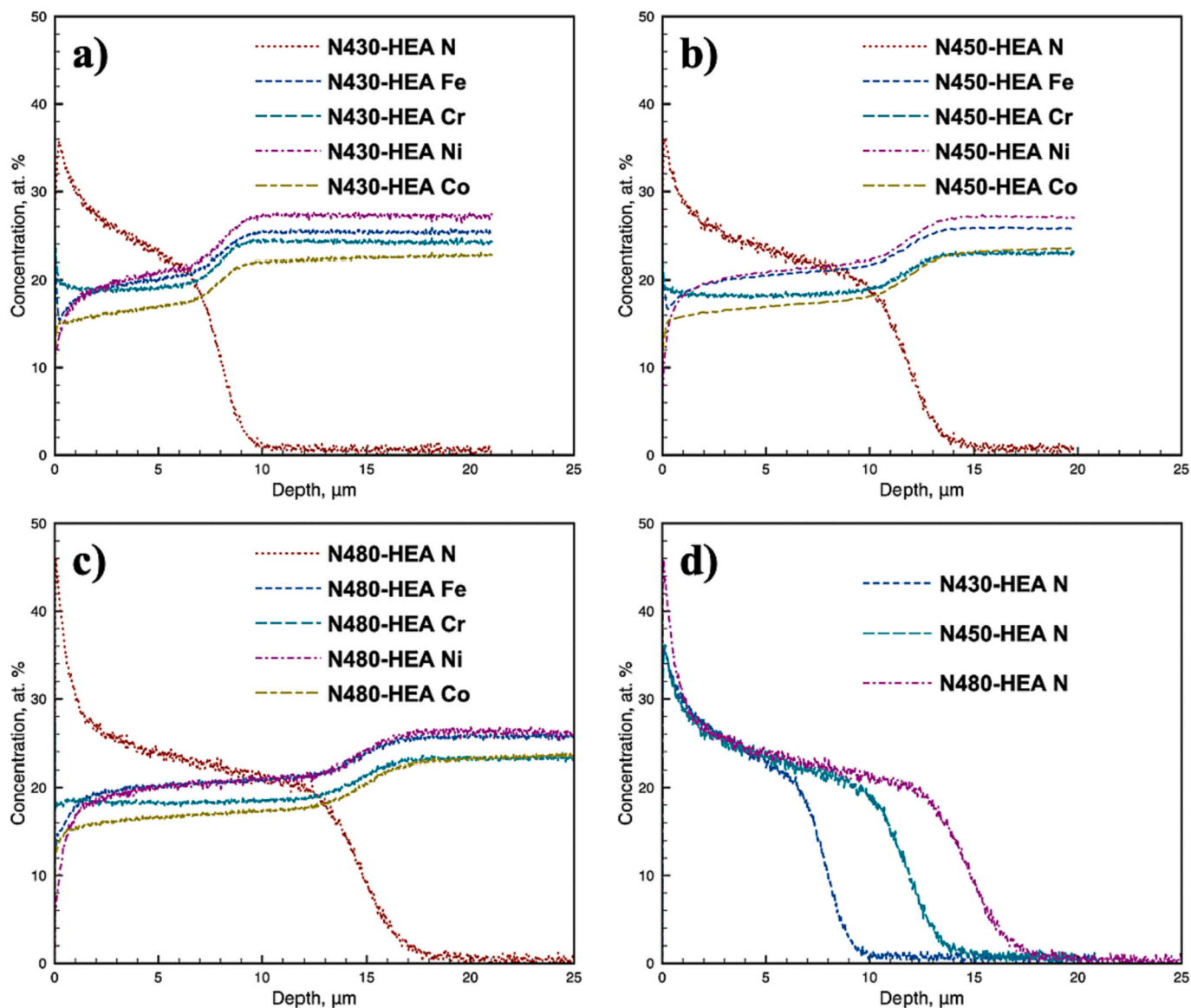
Fig. 2. GDOES composition-depth profiles for the HEA after ASPN treatments at a) 430 °C, b) 450 °C and c) 480 °C; and d) the GDOES nitrogen-depth profiles of all the nitrided samples.

3.4. TEM analysis

BF-TEM in Fig. 4a showed a rather featureless morphology for γ_N in N430-HEA. The SAEDs for γ_N (at 110 and 112 FCC zone axes, Fig. 4b**&d**, respectively) exhibited FCC diffraction spots, indicating an expanded austenitic structure. The absence of expansion anisotropy under SAED was owing to the relaxation of the residual stress (i.e., 'unconstrained' [52]) when the material was lifted from the nitrided surface and thinned to a < 150 nm foil. As a result of the N-induced plastic deformation at the nitrided surface, intersecting shear bands of width ranging at ~25–35 nm were observed within γ_N-HEA grains in N430-HEA (Fig. 4c**&d**). Owing to localised shear deformation, the shear bands gave rise to partial diffraction rings as indicated in Fig. 3c**&d**.

Corresponding to the bright and dark regions in the etched nitrided case in N480-HEA (Fig. 1e), two distinct regions were identified and labelled as Region I and II in Fig. 5a**&d**. HR-TEM in Fig. 5b exhibited a polycrystalline structure for Region I. The corresponding Fast Fourier Transform (FFT) pattern in Fig. 5c matched with CrN and FCC γ-Fe using PDF cards 01–076-2494 and 00–052-0513, respectively. Under STEM-EDS analysis (Fig. 5d**&d1-d5**), Region I is composed of an intimate

mixture of nano-lamellae with thicknesses ranging from ~3–6 nm and lengths ranging from ~5–40 nm. The Cr/N-depleted regions are rich in Fe, Ni and Co (as indicated by circle A in **Fig. 5 d1-d5**). The high-Cr/N regions are depleted in Fe, Ni and Co (as indicated by circle B in **Fig. 5 d1-d5**). Hence, the phase mixture in Region I can be identified as, CrN + γ-(Fe, Ni, Co). Considering its significant Cr segregation (**Fig. 5 d4**), Region I corresponds to the dark regions in the etched treatment case in Fig. 1c**&e**. Analogous cellular mixtures of nano-lamellae were widely reported for γ_N-304/316 at elevated treatment/annealing temperatures [25,53–55], which can result in reduced material corrosion resistance.

On the other hand, corresponding to a bright contrast after etching (Fig. 1e), significant elemental segregation was not measured for Region II under STEM-EDS (**Fig. 5d1-d5**). However, TEM analysis (Fig. 6) indicates two coherent FCC phases for Region II in N480-HEA. As demonstrated by Fig. 6b and the bottom-right inset in Fig. 6d, two FCC phases showed a cube-on-cube orientation relationship. SAED in Fig. 6b suggested a ratio at ~1.12 for the reciprocal d-spacing of the two phases, which is close to ~1.10 between CrN and γ_N. Noticeably, concerning the high-Si nano-precipitates recently revealed in γ_N of a similar morphology [10,25,33], the SEM-EDS analysis in this study indicated no
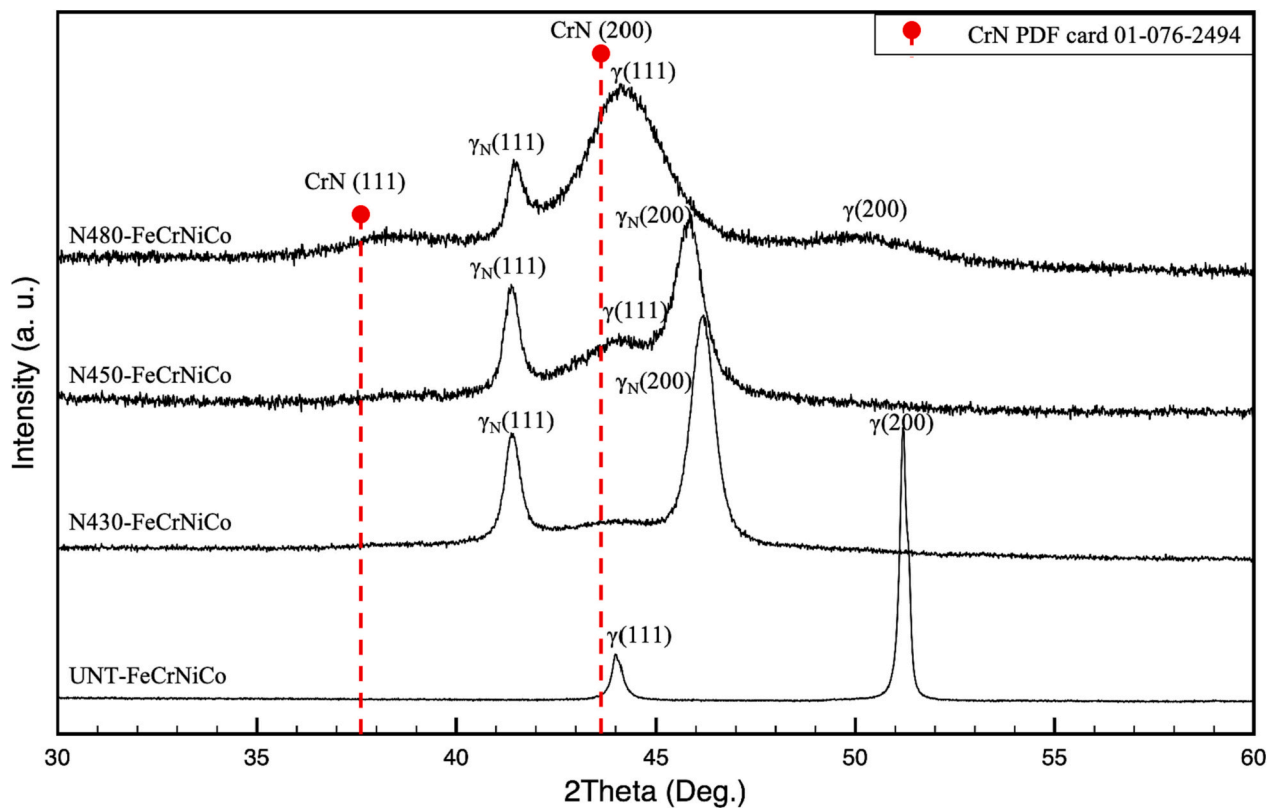
Fig. 3. XRD profiles of HEA before and after ASPN at 430 °C, 450 °C and 480 °C.

measurable Si content in the FeCoNiCr substrate. Si redistribution was also not observed for both Region I and II (Fig. 5) during the STEM-EDS analysis. In this sense, considering also the strong chemical affinity between Cr and N (and the CrN formation in Region I), the microstructure of Region II could be identified as CrN nanoprecipitates in a γ_N matrix. The wavy lattice fringes of γ_N 200 in Region II (top right insets in Fig. 6d) were attributable to the lattice distortion from the fine dot-like CrN nanoprecipitates. The lack of observable elemental redistribution for Region II in STEM-EDS analysis in this study (as shown in **Fig. 5 d1-d5**) could be due to the limited signal contrast that resulted from the small size of the nanoprecipitates (i.e., ~1–3 nm) and their spatial distribution within a relatively thick TEM sample (of approximately 100 nm in thickness).

Additionally, similar to that observed in an equimolar FeCrNi alloy after ASPN treatment [33], a topmost layer was revealed in Fig. 7a for the FIB-TEM sample prepared from the 480 °C ASPN-treated FeCoNiCr, which exhibited nanocrystalline diffraction rings in SAED (Fig. 7b). The diffraction and FFT rings matched with CrN and γ-Fe (using PDF cards 01–076-2494 and 00–052-0513, respectively), as indicated in Fig. 7b**&c**. The measured thickness of the topmost layer ranges at ~350–450 nm for the region revealed from the FIB-TEM sample. The nanocrystalline layer could be associated with accelerated nitride formation at the topmost surface owing to the high substrate Cr level (see discussions in **Section 4.2**).

4. Discussion

4.1. Role of each component on N uptake and non-sluggish interstitial diffusion

The N concentration levels and case depths of the nitrided HEA surfaces have been shown in Fig. 1**&2**. The surface N uptake is strongly influenced by the net chemical environment from the chemical composition of the substrate alloy under equivalent nitriding

treatments. While both Fe-Cr-Ni austenitic SS and FeCoNiCr substrate alloys have an FCC austenitic structure, the FeCoNiCr HEA significantly differs from austenitic SSs (that has been extensively studied under low-temperature nitriding) in substrate chemical composition by i) the introduction of 25 at.% Co and ii) a relatively higher Ni/Cr content. Both the moderate N concentration levels and the considerably thick diffusion cases in the ASPN-treated FeCoNiCr HEA are balanced outcomes between the different equimolar components in the substrate.

Firstly, considering the N concentration ranging at 16–32 at.% (under equivalent ASPN [33]) and 14–38 at.% (after gaseous nitriding [47]) for γ_N-316 case, the γ_N-FeCoNiCr case generated in this study displayed moderate N concentration levels at 20–28 at.%. The drastic change in substrate chemical composition from Fe-18Cr-11Ni (as for austenitic SSs) to equimolar FeCoNiCr did not lead to substantial alteration in surface N concentration level under the selected nitriding conditions. Nevertheless, the increase in Cr content in austenitic Fe-Cr-Ni alloys has been evidently demonstrated to increase the N concentration of the N-modified surface following low-temperature nitriding [23,24,33]. In this sense, the introduction of equimolar Co and the high Ni content in FeCoNiCr appear to offset the effect of the high substrate Cr content on N uptake, resulting in moderate surface N concentration levels.

Secondly, compared with Fe-Cr-Ni SSs under equivalent surface N-modification treatments, the N-modified cases were often found thinner in Co-Cr alloys [56] and Ni-Cr alloys [14,16,22,57]. The addition of equimolar Co and the relatively high Ni concentration in FeCoNiCr HEA was expected to result in case depths thinner than those in Fe-Cr-Ni SSs following equivalent nitriding treatments. However, FeCoNiCr (Table 1) presented rather thick nitrided cases with thicknesses ranging from ~9 to 16 μm, when compared to the ~8–13 μm thick cases in ASPN-treated 316 SS [33]. In this sense, the equimolar Cr could counteract the effect from equimolar Co/Ni to N interstitial diffusion in the quaternary FeCoNiCr HEA. Noticeably, the N concentration levels influence the N diffusivity in expanded austenite and the overall case thickness. For
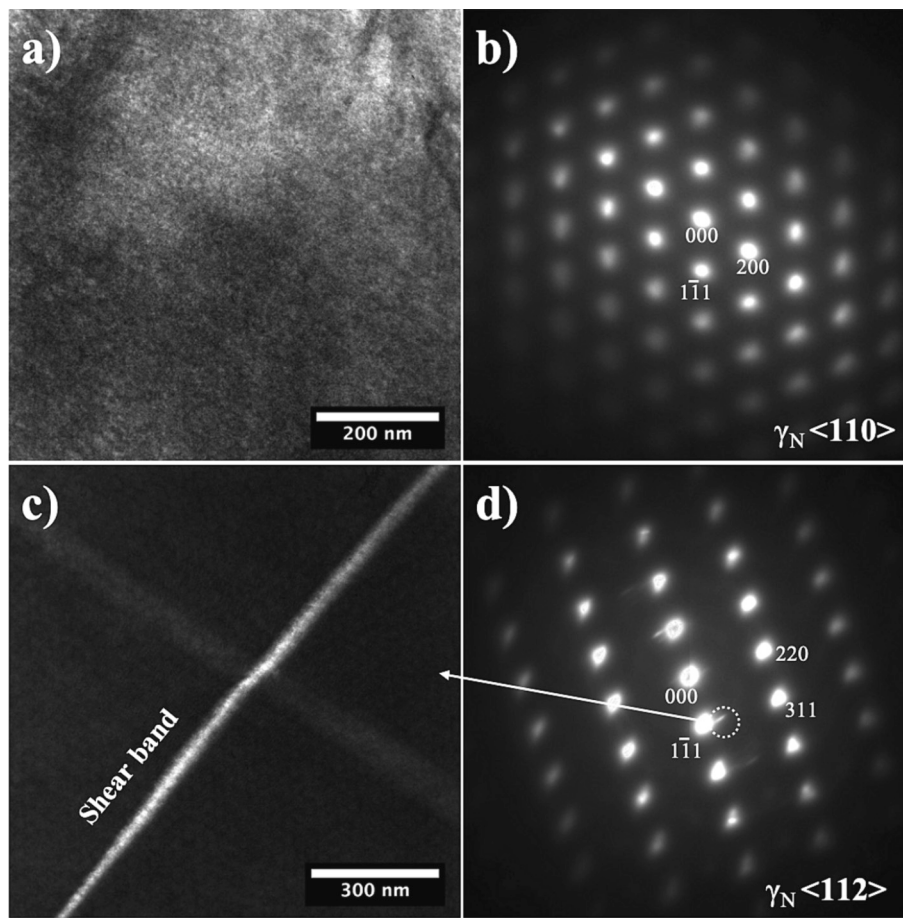
Fig. 4. TEM images and SAED for the primary treatment case in N430-HEA: a) BF-TEM and b) corresponding SAED within an γ$_N$ grain; c) DF-TEM image and d) SAED showing a shear band in γ$_N$ (aperture position is indicated in Fig. 4d).

example, N diffusivity in γ$_N$-316 firstly increases and then decreases with increasing N concentration [58,59]. γ$_N$-316 displayed maximum N diffusivity at N occupancy of ~0.45 over its full N occupancy range of ~0.2–0.6 when nitrided at 445 °C [60]. The relatively thin treatment cases in the ASPN-treated FeNiCr alloy were accompanied by high N interstitial occupancies at ~0.43–0.56 [33]. In this sense, the rather thick treatment cases in the nitrided FeCoNiCr in this study were consistent with its moderate N occupancies at ~0.25–0.39, which seemed to reside near its N diffusivity maxima (that is yet to be confirmed).

Considering the considerably thick treatment cases (Table 1), interstitial diffusion is not sluggish in ASPN-treated FeCoNiCr HEA at ~430–480 °C. Compared with the ~7–12 µm thick treatment cases in a ternary FeNiCr alloy after equivalent ASPN treatments [33], the diffusion depths were thicker at ~9–16 µm in the quaternary FeCoNiCr HEA with an additional equimolar component in this study. In this sense, we may claim that the overall nitrogen interstitial diffusion depth in multicomponent alloys did not become more sluggish with the increased number of components in the equimolar system at the selected treatment conditions at 430–480 °C, which agrees with the statement that "sluggish diffusion effect is independent of the number of elements in the system" for substitutional diffusion at temperatures above 950 °C [41,42].

4.2. Interstitial-induced plasticity in γ$_N$-FeCoNiCr

Analogous to the N-expanded austenite cases in SSs, the low-temperature N-modified HEA surface displayed anisotropic lattice expansion (as demonstrated by XRD peak shifting in Fig. 3) and an austenitic structure (see FCC diffraction reflections in Fig. 4). Moreover, the shear banding (and the absence of martensitic HCP-ε$_N$) in γ$_N$-HEA at 430 °C (Fig. 4c&d) indicated N-induced plastic deformation in the treatment case, as constrained from a bulk core [52]. Considering the threshold SFE at <18–20 mJ m^{-2} for the occurrence of martensitic shear transformation in FCC alloys [61], the presence of shear bands (and the absence of HCP-ε$_N$) correlated well with the room-temperature SFE of the FeCoNiCr HEA (i.e., at 26.8 mJ m^{-2} [36,62]). This is consistent with the SFE-dependent plasticity proposed for N-expanded austenite in SSs [25], where band-like features – i.e., ~10–40 nm thick martensitic ε$_N$ laths in γ$_N$-AG17 and ~ 120 nm wide shear bands in γ$_N$-330 – have been respectively revealed at the surface of a low-SFE (~10–18 mJ m^{-2} [63,64]) alloy AG17 and a high-SFE (> ~ 30 mJ m^{-2}) alloy 330 [10,25,26].

4.3. On the structure evolution in the nitrided surface

Cr-nitride formation is a key indicator of the corrosion resistance of plasma nitrided high-Cr substrate alloys. Firstly, as demonstrated by Fig. 5&6, CrN precipitates can form in the γ$_N$-FeCoNiCr case as i) nano-lamellae at grain boundaries, and ii) nano-dots from within γ$_N$ grains at elevated treatment temperatures. The cellular and dot-like nano-precipitation mechanisms in γ$_N$-FeCoNiCr can be identified as γ$_N$ (+ CrN) → γ + CrN for Region I and γ$_N$ → γ$_N$ + CrN for Region II, respectively. While the cellular CrN precipitation has been often reported for γ$_N$-SSs [25,53–55], the dot-like CrN nanoprecipitates in Region II in γ$_N$-FeCoNiCr were somewhat comparable to the "nanometric CrN precipitates" reported in AISI 304 L [65,66] and the interstitial substitutional CrN "nano-clustering" revealed in Fe-35Ni-Cr alloys [67,68] after
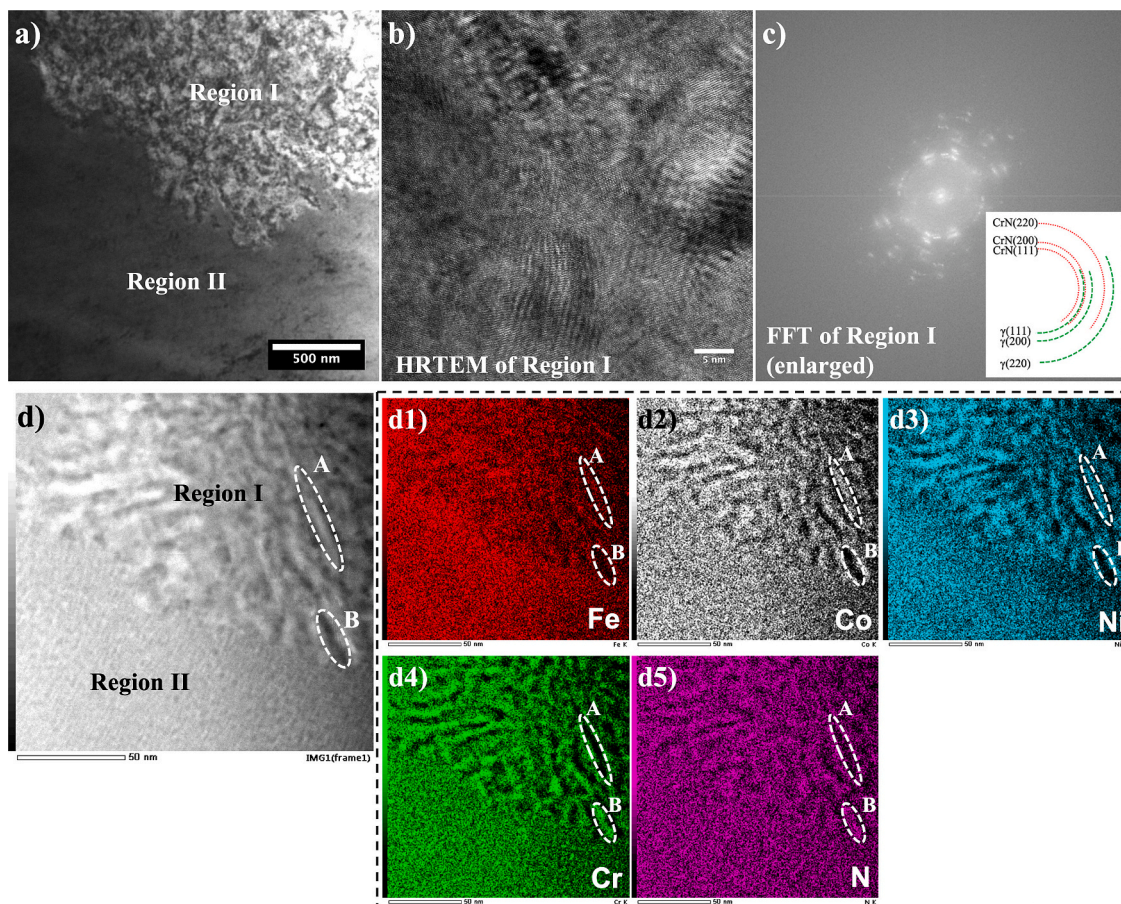
Fig. 5. TEM analysis for the primary treatment case in N480-HEA: a) overview BF-TEM, showing two distinct regions (i.e., Region I and II); b) HR-TEM image and c) enlarged FFT for Region I in Fig. 5b (inset shows the schematic illustration of the indexed FFT pattern); d) local STEM-BF image for both Region I and II, and d1-d5) corresponding STEM-EDS maps for Fe, Co, Ni, Cr, and N, respectively. Two dashed circles highlight features A and B in Region I to guide viewing.

low-temperature N-modification treatments. The CrN formation mechanisms were analogous between γ_N-FeCoNiCr and γ_N-SSs at the selected treatment conditions.

Secondly, the "sluggish diffusion" effect of HEA does not seem to inhibit CrN formation and delay the formation of dark regions in the etched nitrided case. Indeed, the low substitutional diffusivity in HEA [69,70] could limit Cr segregation and CrN formation within γ_N-FeCoNiCr grains. However, significant Cr segregation occurred at grain boundaries via cellular CrN precipitation in the γ_N-FeCoNiCr case (i.e., Region I, Fig. 5 d1-d5), which is most likely controlled by the "non-sluggish" substitutional diffusion in HEAs at grain boundaries [71]. Moreover, compared with the bright γ_N-316 case in 'conventional' 316 SS under equivalent ASPN treatment conditions at 450 °C and 10 h [33], dark regions were observed in the γ_N-FeCoNiCr case (Fig. 1c). In this sense, cellular CrN precipitation occurred more readily in the equimolar FeCoNiCr HEA upon low-temperature nitriding, which could be associated with the high ~25 wt% substrate Cr content.

Furthermore, the ultra-high substrate Cr content at 33 wt% and high surface N levels (e.g., ~28–34.% at 450 °C) in the equivalently ASPN-treated FeCrNi medium entropy alloy should result in even greater potency for CrN formation in the γ_N-FeCrNi case [33]. However, while FeCrNi shows a bright γ_N case after equivalent nitriding treatment at 450 °C [33], early onset of dark regions was observed in the γ_N-FeCoNiCr case (Fig. 1c) in this study. In this sense, the anomalous 'non-cellular' Si-associated nano-precipitation mechanism revealed at the nitrided FeCrNi surface seems to play an important role in prohibiting substantial Cr segregation [33]. Moreover, similar to those high Si nano-precipitates in γ_N-330/FeCrNi [10,33], the dot-like CrN nano-

precipitates in γ_N-FeCoNiCr (i.e., Region II in Fig. 6) also showed a finely-dispersed 'non-cellular' precipitation morphology, leading to a favourable bright appearance after etching. Compared with the ~5–30 nm spheroidal high-Si nanoprecipitates in γ_N-FeCrNi [33] after equivalent ASPN treatment at 480 °C, the dot-like CrN nanoprecipitates in γ_N-FeCoNiCr (in Region II, Fig. 5&6) were much smaller at ~1–3 nm. Similar nano-scale CrN "nano-clustering" [67,68] and "sphere-like" CrN nanoprecipitates [65,66] were also reported in nitrided Fe-Cr-Ni alloys.

As the last point, above the primary treatment case in N480-FeCoNiCr, a ~ 350–450 nm thick topmost nanocrystalline layer was revealed in Fig. 7. In contrast with the cellular precipitation with partial FFT rings (for Region I, Fig. 5) and the dot-like precipitates with cube-on-cube orientation relationship to matrix (for Region II, Fig. 6) in the primary treatment case, this topmost nanocrystalline case exhibited the most pronounced nitride formation. Similar "very high N concentrations" and nanocrystalline layers were also observed in the topmost region in ASPN-treated FeNiCr alloy [33]. As CrN precipitation initiated from the regions of the highest N concentration (usually the topmost surface) during nitriding, the increased defect densities in the nano-precipitated region further enhanced N absorption and nitride formation. Compared to SSs with ~18 wt% Cr, it appears that the high Cr content in the ternary (at ~33 wt%) and quaternary (at ~25 wt%) equimolar alloys tends to promote such a topmost nanocrystalline layer. Noticeably, "very high N concentration" in GDOES profiles has also been observed at the topmost surface of AISI 316 SS under gaseous nitriding when treated at high nitriding potentials (especially at the "infinite nitriding potential" [72]). The formation of such a topmost nano-crystalline layer (with pronounced CrN formation) seems to favour high
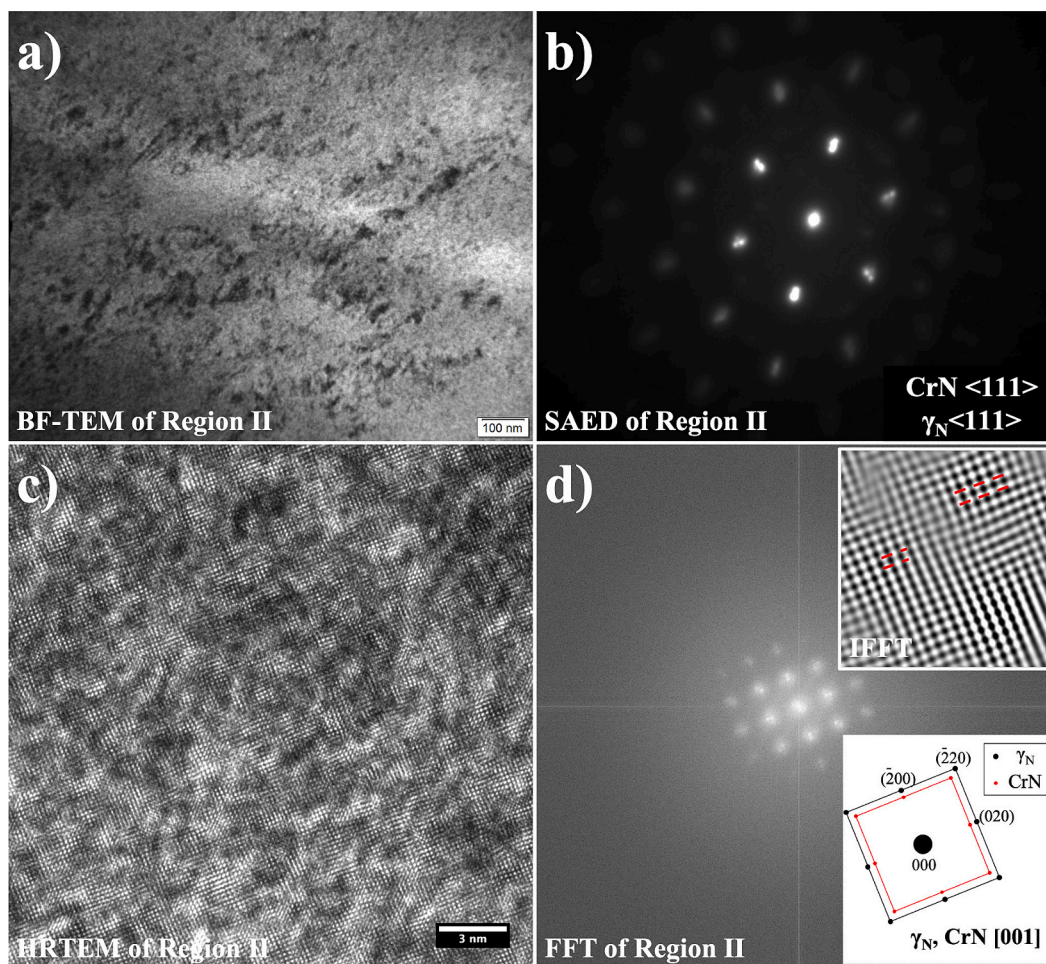
Fig. 6. TEM analysis for Region II in the primary treatment case in N480-FeCoNiCr: a) BF-TEM and b) SAED at FCC 111 zone axis; c) HRTEM and d) corresponding FFT at FCC 001 zone axis (bottom-right insets are schematic of the indexed FFT pattern; top-right inset is enlarged IFFT reconstructed from the γ_N 200 signals).

substrate Cr content and high nitrogen volume fraction in the treatment atmosphere.

5. Conclusions

This work investigated the interstitial absorption and microstructure of a quaternary FeCoNiCr HEA after ASPN treatments at 430–480 °C, which paved the way for future exploration of low-temperature nitriding of HEAs. Conclusions can be drawn as follows,

- Analogous to those in SSs, the γ_N-FeCoNiCr case displayed a bright appearance after etching, anisotropic lattice expansion under XRD, FCC electron diffraction reflections and SFE-dependent plasticity products under TEM, and enhanced surface micro-hardness at ~1300–1400 $HV_{0.025}$. The relatively large case thicknesses at 9–16 μm suggested that interstitial diffusion was not sluggish.
- The nitrided FeCoNiCr surface showed moderate N absorption levels at ~20–28 at.% N. The change in substrate chemical composition from 304/316 SSs (e.g., Fe-18Cr-8/11Ni) to equimolar FeCoNiCr did not significantly alter surface N uptake under selected treatment conditions.
- At 480 °C, three different CrN nanoprecipitation regions were identified, being: i) cellular mixture of ~3–6 nm thick and ~ 5–40 nm wide CrN + γ nano-lamellae, which gives rise to the dark regions (indicating reduced corrosion resistance) in the nitrided case, ii) a fine dispersion of ~1–3 nm 'non-cellular' and (semi-)coherent CrN nanoprecipitates in a γ_N matrix for the residual bright treatment case,

and iii) a ~ 350–450 nm thick nanocrystalline layer composed of γ + CrN, owing to pronounced nitride formation at the topmost surface.
- Despite the sluggish (substitutional) diffusion in the FeCoNiCr HEA, the substantial Cr segregation in the γ_N-FeCoNiCr case (via cellular CrN nanoprecipitation) was predominately controlled by the non-sluggish grain boundary diffusion. Comparing 316 SS (from the previous study) and FeCoNiCr after equivalent ASPN treatment at 450 °C, the cellular CrN formation occurred more readily in γ_N-FeCoNiCr, which is most likely associated with the high 25 at.% Cr in the FeCoNiCr HEA.

CRediT authorship contribution statement

Xiao Tao: Conceptualization, Formal analysis, Investigation, Methodology, Visualization, Writing – original draft, Writing – review & editing. **Yepeng Yang:** Formal analysis, Project administration, Visualization. **Jiahui Qi:** Formal analysis, Investigation, Methodology. **Biao Cai:** Project administration, Resources. **W. Mark Rainforth:** Funding acquisition, Project administration, Resources, Writing – review & editing. **Xiaoying Li:** Methodology, Supervision, Writing – review & editing. **Hanshan Dong:** Funding acquisition, Writing – review & editing.

Declaration of Competing Interest

The authors declare that they have no known competing financial interests or personal relationships that could have appeared to influence
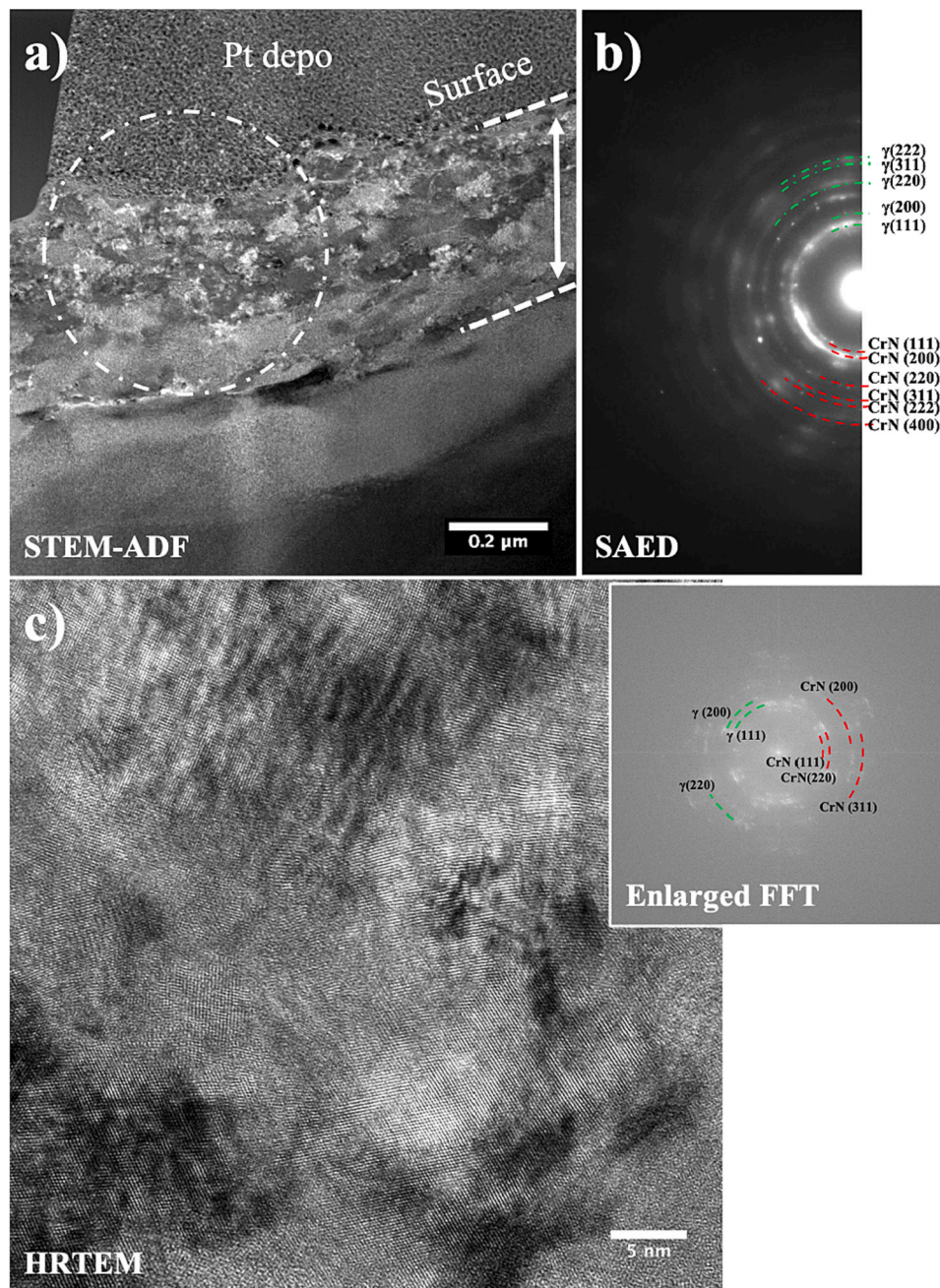

Fig. 7. TEM analysis for the topmost layer in 480 °C ASPN-treated FeCoNiCr: a) annular dark field (ADF) and b) SAED image for overview of the nanocrystalline layer; and c) local HR-TEM image (inset: enlarged FFT). The diffraction aperture position is indicated in Fig. 7a.

the work reported in this paper.

Data availability

Data will be made available on request.

References

[1] Z.L. Zhang, T. Bell, Structure and corrosion resistance of plasma nitrided stainless steel, Surf. Eng. 1 (2) (1985) 131–136.
[2] K. Ichii, K. Fujimura, T. Takase, Structure of the ion-nitrided layer of 18-8 stainless steel, Technology Reports of Kensai University 27, 1986, pp. 135–144.
[3] Y. Sun, T. Bell, Sliding wear characteristics of low temperature plasma nitrided 316 austenitic stainless steel, Wear 218 (1998) 34–42.
[4] T. Bell, Y. Sun, Low-temperature plasma nitriding and carburising of austenitic stainless steels, Heat Treat. Met. 29 (2002) 57–64.
[5] C.X. Li, T. Bell, Corrosion properties of active screen plasma nitrided 316 austenitic stainless steel, Corros. Sci. 46 (2004) 1527–1547.
[6] C.X. Li, T. Bell, Sliding wear properties of active screen plasma nitrided 316 austenitic stainless steel, Wear 256 (11) (2004) 1144–1152.
[7] J.C. Stinville, P. Villechaise, C. Templier, J.P. Riviere, M. Drouet, Plasma nitriding of 316L austenitic stainless steel: experimental investigation of fatigue life and surface evolution, Surf. Coat. Technol. 204 (12) (2010) 1947–1951.

[8] J. Buhagiar, X. Li, H. Dong, Formation and microstructural characterisation of S-phase layers in Ni-free austenitic stainless steels by low-temperature plasma surface alloying, Surf. Coat. Technol. 204 (3) (2009) 330–335.

[9] F. Borgioli, A. Fossati, G. Matassini, E. Galvanetto, T. Bacci, Low temperature glow-discharge nitriding of a low nickel austenitic stainless steel, Surf. Coat. Technol. 204 (21) (2010) 3410–3417.

[10] X. Tao, X. Li, H. Dong, A. Matthews, A. Leyland, Evaluation of the sliding wear and corrosion performance of triode-plasma nitrided Fe-17Cr-20Mn-0.5N high-manganese and Fe-19Cr-35Ni-1.2Si high-nickel austenitic stainless steels, Surf. Coat. Technol. 409 (2021) 126890.

[11] X.Y. Li, N. Habibi, H. Dong, Microstructural characterisation of a plasma carburised low carbon Co-Cr alloy, Surf. Eng. 23 (1) (2007) 45–51.

[12] R. Liu, X. Li, X. Hu, H. Dong, Surface modification of a medical grade Co-Cr-Mo alloy by low-temperature plasma surface alloying with nitrogen and carbon, Surf. Coat. Technol. 232 (2013) 906–911.

[13] Z. Ren, S. Eppell, S. Collins, F. Ernst, Co–Cr–Mo alloys: improved wear resistance through low-temperature gas-phase nitro-carburization, Surf. Coat. Technol. 378 (2019) 124943.

[14] X. Tao, J. Kavanagh, X. Li, H. Dong, A. Matthews, A. Leyland, An investigation of precipitation strengthened Inconel 718 superalloy after triode plasma nitriding, Surf. Coat. Technol. 128401 (2022).

[15] S. Chollet, L. Pichon, J. Cormier, J.B. Dubois, P. Villechaise, M. Drouet, A. Declemy, C. Templier, Plasma assisted nitriding of Ni-based superalloys with various microstructures, Surf. Coat. Technol. 235 (2013) 318–325.

[16] K.M. Eliasen, T.L. Christiansen, M.A.J. Somers, Low temperature gaseous nitriding of Ni based superalloys, Surf. Eng. 26 (4) (2010) 248–255.

[17] Y. Sun, Kinetics of layer growth during plasma nitriding of nickel based alloy Inconel 600, J. Alloys Compd. 351 (2003) 241–247.

[18] C. Leroy, T. Czerwiec, C. Gabet, T. Belmonte, H. Michel, Plasma assisted nitriding of Inconel 690, Surf. Coat. Technol. 142-144 (2001) 214–247.

[19] Y. Cao, F. Ernst, G.M. Michal, Colossal carbon supersaturation in austenitic stainless steels carburized at low temperature, Acta Mater. 51 (2003) 4171–4181.

[20] T. Christiansen, M.A.J. Somers, Decomposition kinetics of expanded austenite with high nitrogen content Zeitschrift fur Metallkunde 421, 2006, pp. 181–189.

[21] T. Bell, C.X. Li, Plasma thermochemical processing of austenitic stainless steel for combined wear and corrosion resistance, SAE Technical Paper, 2002, 2002-01-1337.

[22] D.L. Williamson, J.A. Davis, P.J. Wilbur, Effect of austenitic stainless steel composition on low-energy, high-flux nitrogen ion beam processing, Surf. Coat. Technol. 103-104 (1998) 178–184.

[23] H.L. Che, S. Tong, K.S. Wang, M.K. Lei, M.A.J. Somers, Co-existence of γ'N phase and γN phase on nitrided austenitic Fe-Cr-Ni alloys – I. Experiment, Acta Mater. 177 (2019) 35–45.

[24] X. Tao, A. Matthews, A. Leyland, On the nitrogen-induced lattice expansion of a non-stainless austenitic steel, Invar 36®, under triode plasma nitriding, Metall. Mater. Trans. A 51 (1) (2020) 436–447.

[25] X. Tao, X. Liu, A. Matthews, A. Leyland, The influence of stacking fault energy on plasticity mechanisms in triode-plasma nitrided austenitic stainless steels: implications for the structure and stability of nitrogen-expanded austenite, Acta Mater. 164 (2019) 60–75.

[26] X. Tao, J. Qi, M. Rainforth, A. Matthews, A. Leyland, On the interstitial induced lattice inhomogeneities in nitrogen-expanded austenite, Scr. Mater. 185 (2020) 146–151.

[27] H. Dong, S-phase surface engineering of Fe-Cr, Co-Cr and Ni-Cr alloys, Int. Mater. Rev. 55 (2) (2010) 65–98.

[28] B. Cantor, I.T.H. Chang, P. Knight, A.J.B. Vincent, Microstructural development in equiatomic multicomponent alloys, Mater. Sci. Eng. A 375–377 (2004) 213–218.

[29] J.W. Yeh, S.K. Chen, S.J. Lin, J.Y. Gan, T.S. Chin, T.T. Shun, C.H. Tsau, S.Y. Chang, Nanostructured high-entropy alloys with multiple principal elements: novel alloy design concepts and outcomes, Adv. Eng. Mater. 6 (5) (2004) 299–303.

[30] A. Gali, E.P. George, Tensile properties of high- and medium-entropy alloys, Intermetallics 39 (2013) 74–78.

[31] Y. Zhang, T. Zuo, Y. Cheng, P.K. Liaw, High-entropy alloys with high saturation magnetization, electrical resistivity and malleability, Sci. Rep. 3 (1) (2013) 1455.

[32] Y.F. Ye, Q. Wang, J. Lu, C.T. Liu, Y. Yang, High-entropy alloy: challenges and prospects, Mater. Today 19 (6) (2016) 349–362.

[33] X. Tao, Y. Yang, J. Qi, B. Cai, W.M. Rainforth, X. Li, H. Dong, Active screen plasma nitriding of a Si-alloyed FeCrNi medium entropy alloy: high interstitial absorption and an anomalous Si-induced decomposition mechanism in N-expanded austenite, Appl. Surf. Sci. 624 (2023) 157137.

[34] Y. Peng, J. Gong, T.L. Christiansen, M.A.J. Somers, Surface modification of CoCrFeNi high entropy alloy by low-temperature gaseous carburization, Mater. Lett. 283 (2021) 128896.

[35] A. Nishimoto, T. Fukube, T. Maruyama, Microstructural, mechanical, and corrosion properties of plasma-nitrided CoCrFeMnNi high-entropy alloys, Surf. Coat. Technol. 376 (2019) 52–58.

[36] A.J. Zaddach, C. Niu, C.C. Koch, D.L. Irving, Mechanical properties and stacking fault energies of NiFeCrCoMn high-entropy alloy, JOM 65 (12) (2013) 1780–1789.

[37] B. Cai, B. Liu, S. Kabra, Y. Wang, K. Yan, P.D. Lee, Y. Liu, Deformation mechanisms of Mo alloyed FeCoCrNi high entropy alloy: in situ neutron diffraction, Acta Mater. 127 (2017) 471–480.

[38] Y. Wang, B. Liu, K. Yan, M. Wang, S. Kabra, Y.-L. Chiu, D. Dye, P.D. Lee, Y. Liu, B. Cai, Probing deformation mechanisms of a FeCoCrNi high-entropy alloy at 293 and 77 K using in situ neutron diffraction, Acta Mater. 154 (2018) 79–89.

[39] L. Tang, K. Yan, B. Cai, Y. Wang, B. Liu, S. Kabra, M.M. Attallah, Y. Liu, Deformation mechanisms of FeCrCrNiMo0.2 high entropy alloy at 77 and 15 K, Scr. Mater. 178 (2020) 166–170.

[40] J.W. Yeh, Recent progress in high-entropy alloys, Annales de Chimie Science des Materiaux (Paris) 31 (6) (2006) 633–648.

[41] J. Dąbrowa, M. Zajusz, W. Kucza, G. Cieślak, K. Berent, T. Czeppe, T. Kulik, M. Danielewski, Demystifying the sluggish diffusion effect in high entropy alloys, J. Alloys Compd. 783 (2019) 193–207.

[42] W. Kucza, J. Dąbrowa, G. Cieślak, K. Berent, T. Kulik, M. Danielewski, Studies of "sluggish diffusion" effect in Co-Cr-Fe-Mn-Ni, Co-Cr-Fe-Ni and Co-Fe-Mn-Ni high entropy alloys; determination of tracer diffusivities by combinatorial approach, J. Alloys Compd. 731 (2018) 920–928.

[43] K.-Y. Tsai, M.-H. Tsai, J.-W. Yeh, Reply to comments on "Sluggish diffusion in Co-Cr-Fe-Mn-Ni high-entropy alloys" by K.Y. Tsai, M.H. Tsai and J.W. Yeh, Acta Materialia 61 (2013) 4887-4897, Scr. Mater. 135 (2017) 158–159.

[44] A. Paul, Comments on "Sluggish diffusion in Co–Cr–Fe–Mn–Ni high-entropy alloys" by K.Y. Tsai, M.H. Tsai and J.W. Yeh, Acta Materialia 61 (2013) 4887–4897, Scr. Mater. 135 (2017) 153–157.

[45] M. Vaidya, S. Trubel, B.S. Murty, G. Wilde, S.V. Divinski, Ni tracer diffusion in CoCrFeNi and CoCrFeMnNi high entropy alloys, J. Alloys Compd. 688 (2016) 994–1001.

[46] S. Corujeira Gallo, H. Dong, Study of active screen plasma processing conditions for carburising and nitriding austenitic stainless steel, Surf. Coat. Technol. 203 (24) (2009) 3669–3675.

[47] T. Christiansen, M.A.J. Somers, Controlled dissolution of colossal quantities of nitrogen in stainless steel, Metall. Mater. Trans. A 37A (2006) 675–682.

[48] Y. Sun, X.Y. Li, T. Bell, X-ray diffraction characterisation of low temperature plasma nitrided austenitic stainless steels, J. Mater. Sci. 34 (1999) 4793–4802.

[49] J.C. Stinville, P. Villechaise, C. Templier, J.P. Riviere, M. Drouet, Lattice rotation induced by plasma nitriding in a 316L polycrystalline stainless steel, Acta Mater. 58 (2010) 2814–2821.

[50] C. Templier, J.C. Stinville, P. Villechaise, P.O. Renault, G. Abrasonis, J.P. Riviere, A. Martinavicius, M. Drouet, On lattice plane rotation and crystallographic structure of the expanded austenite in plasma nitrided AISI 316L steel surf, Coat. Technol. 204 (2010) 2551–2558.

[51] J.C. Stinville, J. Cormier, C. Templier, P. Villechaise, Modeling of the lattice rotations induced by plasma nitriding of 316L polycrystalline stainless steel, Acta Mater. 83 (2015) 10–16.

[52] H.L. Che, M.K. Lei, Microstructure of perfect nitrogen-expanded austenite formed by unconstrained nitriding, Scr. Mater. 194 (2021) 113705.

[53] X.L. Xu, L. Wang, Z.W. Yu, Z.K. Hei, Microstructural characterization of plasma nitrided austenitic stainless steel, Surf. Coat. Technol. 132 (2) (2000) 270–274.

[54] X.Y. Li, Y. Sun, Transmission electron microscopy study of S phase in low temperature plasma nitrided 316 stainless steel, in: T. Bell, K. Akamatsu (Eds.), Stainless Steel 2000: Thermochemical Surface Engineering of Stainless Steel, Maney Publishing, London, 2001, pp. 215–228.

[55] T. Christiansen, M.A.J. Somers, Decomposition kinetics of expanded austenite with high nitrogen contents, Z. Metallkd. 97 (1) (2006) 79–88.

[56] J. Lutz, J.W. Gerlach, S. Mandl, PIII nitriding of fcc-alloys containing Ni and Cr, Phys. Status Solidi A 205 (4) (2008) 980–984.

[57] D. Manova, S. Mandl, H. Neumann, B. Rauschenbach, Formation of metastable diffusion layers in Cr-containing iron, cobalt and nickel alloys after nitrogen insertion, Surf. Coat. Technol. 312 (2017) 81–90.

[58] S. Mändl, F. Scholze, H. Neumann, B. Rauschenbach, Nitrogen diffusivity in expanded austenite, Surf. Coat. Technol. 174-175 (2003) 1191–1195.

[59] S. Mändl, B. Rauschenbach, Concentration dependent nitrogen diffusion coefficient in expanded austenite formed by ion implantation, J. Appl. Phys. 91 (12) (2002) 9737–9742.

[60] T. Christiansen, K.V. Dahl, M.A.J. Somers, Nitrogen diffusion and nitrogen depth profiles in expanded austenite: experimental assessment, numerical simulation and role of stress, Mater. Sci. Technol. 24 (2) (2008) 159–167.

[61] L. Mosecker, A. Saeed-Akbari, Nitrogen in chromium-manganese stainless steels: a review on the evaluation of stacking fault energy by computational thermodynamics, Sci. Technol. Adv. Mater. 14 (2013) 033001.

[62] A.J. Zaddach, R.O. Scattergood, C.C. Koch, Tensile properties of low-stacking fault energy high-entropy alloys, Mater. Sci. Eng. A 636 (2015) 373–378.

[63] R.E. Schramm, R.P. Reed, Stacking fault energies of seven commercial austenitic stainless steels, Metall. Mater. Trans. A 6A (1975) 1345.

[64] J. Talonen, H. Hanninen, Formation of shear bands and strain-induced martensite during plastic deformation of metastable austenitic stainless steels, Acta Mater. 55 (2007) 6108–6118.

[65] A. Martinavičius, R. Danoix, M. Drouet, C. Templier, B. Hannoyer, F. Danoix, Atom probe tomography characterization of nitrogen induced decomposition in low temperature plasma nitrided 304L austenitic stainless steel, Mater. Lett. 139 (2015) 153–156.

[66] A. Martinavičius, G. Abrasonis, A.C. Scheinost, R. Danoix, F. Danoix, J.C. Stinville, G. Talut, C. Templier, O. Liedke, S. Gemming, W. Möller, Nitrogen interstitial diffusion induced decomposition in AISI 304L austenitic stainless steel, Acta Mater. 60 (10) (2012) 4065–4076.

[67] Y. Xie, G. Miyamoto, T. Furuhara, Nanosized Cr-N clustering in expanded austenite layer of low temperature plasma-nitrided Fe-35Ni-10Cr alloy, Scr. Mater. 213 (2022) 114637.

[68] Y. Xie, G. Miyamoto, T. Furuhara, High-throughput investigation of Cr-N cluster formation in Fe-35Ni-Cr system during low-temperature nitriding, Acta Mater. 118921 (2023).

[69] K.Y. Tsai, M.H. Tsai, J.W. Yeh, Sluggish diffusion in Co–Cr–Fe–Mn–Ni high-entropy alloys, Acta Mater. 61 (13) (2013) 4887–4897.

[70] Y. Zhang, T.T. Zuo, Z. Tang, M.C. Gao, K.A. Dahmen, P.K. Liaw, Z.P. Lu, Microstructures and properties of high-entropy alloys, Prog. Mater. Sci. 61 (2014) 1–93.

[71] M. Vaidya, K.G. Pradeep, B.S. Murty, G. Wilde, S.V. Divinski, Radioactive isotopes reveal a non sluggish kinetics of grain boundary diffusion in high entropy alloys, Sci. Rep. 7 (1) (2017) 12293.

[72] T.L. Christiansen, M.A.J. Somers, Low-temperature gaseous surface hardening of stainless steel: the current status, Int. J. Mater. Res. 100 (10) (2009) 1361–1377.